Int J Adv Manuf Technol (2010) 51:659–669
DOI 10.1007/s00170-010-2659-6

ORIGINAL ARTICLE

Effect of path planning on the laser powder deposition process: thermal and structural evaluation

Ehsan Foroozmehr · Radovan Kovacevic

Received: 8 July 2009 / Accepted: 6 April 2010 / Published online: 23 April 2010

Abstract In this study, ANSYS finite element software is used to simulate the temperature and stress field in the laser powder deposition process. The model is used to determine the effect of the deposition pattern on the final stress distribution. Four deposition patterns are defined to cover the same area: long bead, short bead, spiral in, and spiral out. The results show that the deposition pattern significantly affects the temperature history of the process, and consequently, the stress distribution. Among the four deposition patterns, the spiral-in pattern shows the highest and the short-bead pattern shows the lowest maximum residual stress. The modeling results are verified with experiments.

Keywords Finite element method · Laser powder deposition · Residual stress · Deposition pattern

1 Introduction

Laser cladding is shown to be a cost-effective alternative to the conventional surface-modification processes and repair such as plasma spray and mechanical processing. In this process, the laser beam is used to melt metal powder and a thin layer of the substrate to form a metallurgical bond between the deposited layer and the substrate. The laser deposition head can be positioned by a robot arm or a computer numerical controlled (CNC) machine in order to build a 3D component in a layer-wise manner following the path planning instructions from a computer-aided design model [1]. In order to reach the desired geometry of the buildup, a closed-loop control system can be used in which the shape of the molten pool or the height of the deposited bead is monitored during the process [2, 3]. More details regarding the laser cladding process can be found in Refs. [4, 5].

Because of the local high intensity power of the laser beam during the laser cladding process, thermal distortion, and residual stress are usually inevitable. The dominant load that induces residual stress in the material is the thermal load. The thermal expansion of the material locally increases the material volume under the heat source, and because of the high temperature gradient, the neighboring regions cannot deform with the same rate. Therefore, a high stress region is formed around the molten pool that may induce a plastic deformation in the material. In addition, the mismatch of the thermal expansion coefficients between the deposited material and the substrate or within different elements of a composite powder may influence the residual stress as well. It is well-known that the presence of residual stress affects the performance of the structure by causing fatigue, brittle fracture, or stress corrosion cracking [6].

Many efforts have been made to model the laser cladding process including the thermal and structural analysis from the 1D model by Kahlen and Kan [7] to the 2D model by Deus and Mazumder [8] and Vasinonta et al. [9, 10], and the 3D model by Labudovic et al. [11], Dai and Shaw [12], and Costa et al. [13, 14]. The effect of different parameters is studied such as preheating the substrate [15], post-heating the deposited material [11, 16, 17], and the deposition pattern [18]. Nonetheless, most of the published papers in this area, such as Refs. [19, 20], investigate the feasibility of using numerical simulation in

E. Foroozmehr · R. Kovacevic (✉)
Center for Laser Aided Manufacturing (CLAM),
Southern Methodist University,
Dallas, TX, USA
e-mail: kovacevi@engr.smu.edu

predicting the residual stress in the deposited part in a particular situation.

Modeling a complex process like the stress formation in the laser powder deposition (LPD) process requires some simplifying assumptions in order to reduce its computational cost. The level of accuracy of the assumptions is defined by experimental validations. Nickel et al. [18] ignore the additive nature of the process, and in fact, the laser treatment of the substrate is studied. The deflection results are compared by the numerical model, showing acceptable agreement. Kahlen and Kar [7] use a simple 1D model based on Hook's law to predict the residual stress. The residual stress is not measured directly in their study; however, the measured and nominal yield strength shows a good agreement. The majority of researchers use similar assumptions for the material model and the process simulation: an uncoupled thermo-mechanical model is defined in which the temperature history is considered as the load for the mechanical analysis. However, Gosh and Choi [21–23] propose a metallo-thermo-mechanical model in which the thermal microscopic residual stresses that result from microstructure transformations are considered beside the well-known thermal macroscopic residual stresses. In these studies, the volume dilatation and transformation plasticity strain rates are considered in addition to elastic, plastic, and thermal strain rates. The results of the simulations show a noticeable difference between the models considering the microstructure transformations and the ones not considering this effect. The experimental results in Ref. [22] show that by considering the volume strain and transformation plasticity, a better result is obtained. A similar approach in Ref. [21], however, shows that without considering these effects, the experimental and modeled results have a better agreement. This is explained by the fact that the volume strain and the transformation plasticity are considered separately in spite of their dependency in real situations. Nonetheless, considering the complex metallo-thermo-mechanical model seems to be more important for high strength, ferritic or martensitic stainless steels, and less important for low alloy and mild steels [24, 25].

One of the important process parameters of the LPD process is the deposition pattern. It affects the temperature history, and consequently, affects the microstructural and mechanical properties of the deposited material [26]. In the present study, the effect of the deposition pattern on the residual stress formation of the LPD process is investigated. A thermo-mechanical model is used to analyze the temperature and stress field during the deposition process of the material AISI 4140 on a substrate of the same material. ANSYS finite element software is used to simulate the deposition process in order to define the temperature history and the induced stresses due to temperature. The results are validated by experimental study.

2 Model description

The laser powder deposition process consists of the continuous movement of laser beam over the substrate and simultaneously, melting powder particles and the substrate to form a deposition bead. In order to model the process, the continuous movement of the laser beam is divided into small increments, called time steps, and the governing equations are solved as a stationary model for each time step. The results of each time step are used as initial conditions for the next one. The additive nature of the process is introduced by the element birth/death option in ANSYS. In this method, the cladding layer elements are defined at the beginning of the process. However, they are deactivated by multiplying their stiffness by a severe reduction factor [27]. The elements of the cladding layer under laser beam boundary conditions are activated by removing the multiplier at the corresponding time step; then, the thermal or structural analysis is performed and the results are used as the boundary conditions for the next time step. This process continues according to the deposition pattern defined by ANSYS parametric design language (APDL) until the last time step.

Figure 1 shows the image taken during the deposition process. A high-speed camera is assisted by a green laser to capture the image of the molten pool. The glare of the molten pool is eliminated with the aid of proper optical filters. More information about the imaging technique can be found in Ref. [28]. As can be seen in Fig. 1, the laser beam melts partially the substrate and the powder particles (particles cannot be seen in this image) to form the deposition bead. The schematic of this process is shown in Fig. 2. The molten pool is divided into two sections: the leading half in which the substrate is melted and the trailing half in which the particles are melted and the clad is formed. This idea is used in defining the finite element model in Fig. 3. As shown in this figure, four regions can be distinguished: the white elements representing the substrate, the light gray elements representing the already

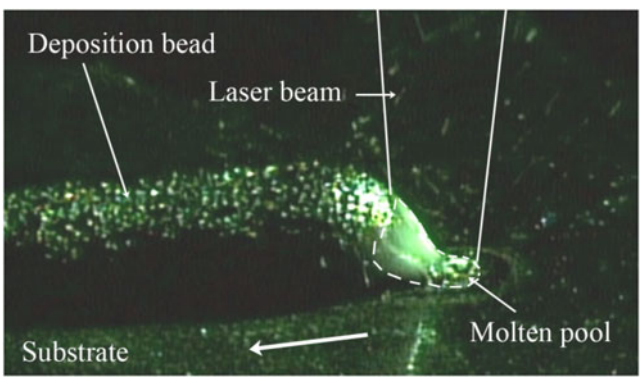

Fig. 1 Image of the molten pool taken during the deposition process

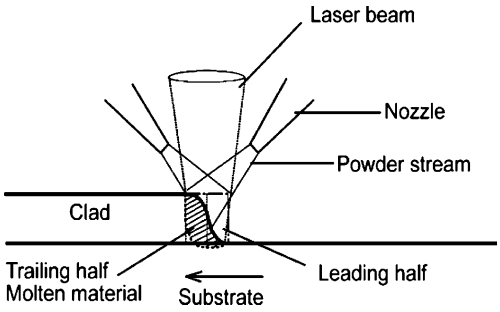

Fig. 2 Schematic of the laser powder deposition process

activated elements of the clad, the dark gray elements representing the activated elements in the current time step that contain the molten feeding material, and the dotted region representing the leading half with the laser heat flux boundary condition. In the present study, the laser scanning speed is 10 mm/s, and the powder feeding rate is 3 g/min with a powder efficiency of 20%. Therefore, with a time step of 25 ms, a set of four elements having the dimensions of 0.25×0.25×0.20 mm is activated (highlighted in Fig. 4). The area on which the heat flux is activated is 0.25×0.50 mm^2. The deposition pattern is then defined by activating the corresponding elements along the deposition path. Figure 5 shows the four deposition patterns with which a similar area is covered on the substrate.

Modeling the LPD process to analyze residual stress consists of two steps: analyzing the heat transfer during the process, and analyzing the stress formation during the process by applying the results of the thermal analysis in the previous step to the model.

2.1 Thermal model

As mentioned, the laser beam in the LPD process strikes the substrate and melts the powder particles. The bead is formed continuously by moving the laser beam over the surface. The temperature field is calculated by solving the 3D heat condsuction moving heat source equation shown in Eq. 1.

$$\rho c_p \frac{\partial T}{\partial t} - \rho c_p \nabla(UT) - \nabla.(K\nabla T) = Q \tag{1}$$

where ρ, c_p, and K are the density, heat capacity, and thermal conductivity, respectively. U is the heat source speed and Q is the heat generation that is not considered in this analysis. As mentioned with the finite element method, the moving heat source is not directly considered. However, the continuous addition of the material to the substrate is divided into many small time steps, and for each time step, a stationary heat transfer equation is solved. The APDL subroutine defines the position of the laser beam at a given time step as a function of U and the beam diameter. Therefore, Eq. 1 is simplified to Eq. 2 and should be solved for each time step with its corresponding boundary conditions.

$$\rho c_p \frac{\partial T}{\partial t} - \nabla.(K\nabla T) = Q \tag{2}$$

The boundary conditions are:

$$-K(\nabla T.n)|_{\xi} = \begin{cases} -h(T-T_0) - \varepsilon\sigma\left(T^4 - T_0^4\right)|_{\xi} & \xi \in \text{molten pool} \\ -h(T-T_0)|_{\xi} & \xi \in \text{substrate surfaces} \end{cases} \tag{3}$$

Where h is the convection heat transfer, and ε and σ are the radiation coefficient and Stephen Boltzmann constant, respectively. The shielding gas effect beside the radiation from the molten pool is considered in the boundary condition of the molten pool. All sides of the substrate have a convection heat transfer boundary condition. The conditions of Eq. 4 should also be satisfied:

$$T(x,y,z,0) = T(x,y,z,\infty) = T_0 \tag{4}$$

The material properties are defined to be temperature dependent, and the latent heat of fusion is considered in the definition of specific heat (Table 1).

2.2 Structural model

The total strain can be written as the sum of the individual components of the strain:

$$\varepsilon_{kl} = \varepsilon_{kl}^E + \varepsilon_{kl}^P + \varepsilon_{kl}^T \qquad (k,l = 1,2,3) \tag{6}$$

Where ε^E, ε^P, and ε^T are the elastic, plastic, and thermal strains, respectively. The transformation plasticity and

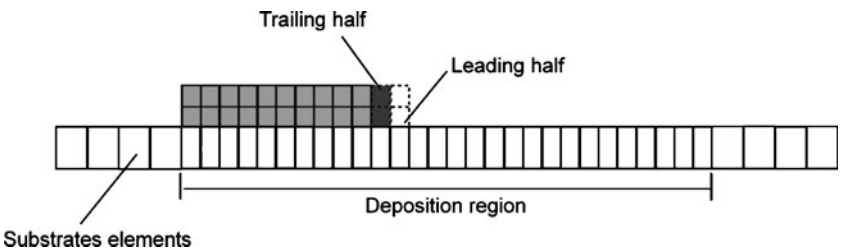

Fig. 3 Finite element model for the deposition process

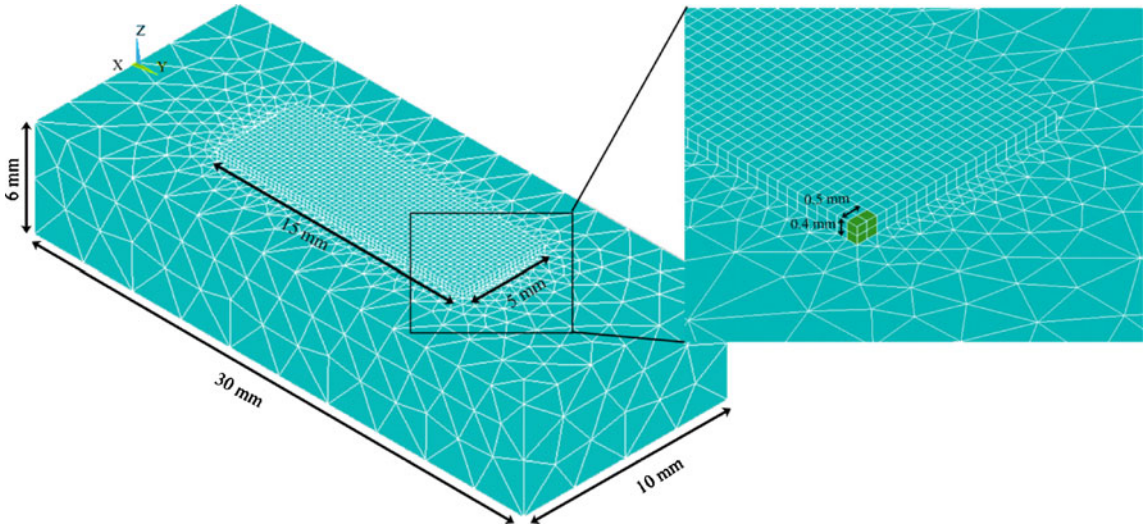

Fig. 4 Finite element model of the substrate and deposition region for one-layer cladding; the first activated set of elements is shown in a higher magnification

volume dilatation strains are not considered in this model. The elastic and thermal strains are expressed as [13]:

$$\varepsilon_{ij}^{E} = \frac{1+\nu}{E}\sigma_{ij} - \frac{\nu}{E}\sigma_{kk}\delta_{ij} \tag{7}$$

$$\varepsilon_{ij}^{T} = \alpha(T - T_i)\delta_{ij} \tag{8}$$

Where ν is Poisson's ratio, E is the elastic modulus, σ_{ij} is the stress tensor, α is the coefficient of thermal expansion, and δ_{ij} is the Kronecker delta that is equal to zero unless the i and j indices are the same, in which the delta is equal to one. T_i is the reference temperature with which the thermal strain is calculated. This temperature is equal to room temperature for the substrate. However, for the activated elements representing the deposited material, considering the same reference temperature as the substrate causes significant errors. It is shown by Neto and Vilar [29] that the absorbed energy from the flying powder particles can be sufficient for the elements to reach their melting temperature before entering the molten pool. Immediately after the solidification starts, the material starts to shrink. Therefore, the T_i for the elements of the deposited material is considered to be equal to the melting temperature, T_m.

The plastic strain is reduced to the form [30]:

$$\varepsilon_{ij}^{P} = \hat{G}\left(\frac{\partial F}{\partial \sigma_{kl}}\sigma_{kl} + \frac{\partial F}{\partial T}T\right)\frac{\partial F}{\partial \sigma_{ij}} \tag{9}$$

With a yield function of:

$$F = F\left(\sigma_{ij}, \varepsilon^{P}, \kappa, T\right) \tag{10}$$

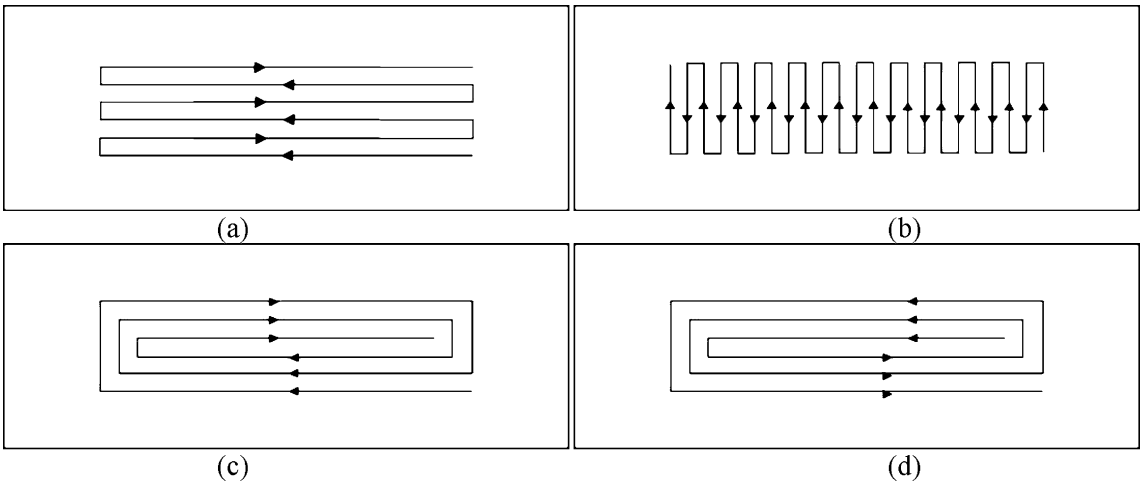

Fig. 5 Schematic presentation of deposition patterns; **a** long beads, **b** short beads, **c** spiral in, **d** spiral out

Table 1 Thermal properties of AISI 4140

Temperature (°C)	25	200	600	700	800	900	1,315	1,450	1,500
Specific heat	473	527	723	821	823	624	607	1,800	607
Density	7,760	7,650	7,580	7,550	7,200	7,150	7,100	7,000	6,900
Conductivity	54.1	48.6	38.5	36.5	34.7	33	30.1	30	30

In which $\hat{G}$ is known as the hardening function:

$$\frac{1}{\hat{G}} = -\left(\frac{\partial F}{\partial \sigma_{mn}^{P}} + \frac{\partial F}{\partial \kappa}\sigma_{mn}\right)\frac{\partial F}{\partial \sigma_{mn}} \tag{11}$$

κ is known as the hardening parameter or plastic work and can be expressed as:

$$\kappa = \sigma_{ij}\dot{\varepsilon}_{ij}^{P} \tag{12}$$

The stress analysis during the process is assumed to be rate independent; meaning the plastic strain forms instantaneously after the stress exceeds the yield stress [31]. For the residual stress analysis, the temperature-dependent properties of the coefficient of thermal expansion, α, the elastic modulus, E, Poisson's ration, ν, and the yield strength, σ_y are required to be defined (Table 2). The material model is assumed to be a temperature-dependent elastoplastic with a tangent modulus of about 1/50 of the Young modulus (Fig. 6).

The substrate is assumed to be stress free at the beginning of the process, and only the thermal load calculated in the last step is applied to the model. The bottom of the substrate is subjected to a zero vertical displacement constraint.

2.3 Model assumptions

The assumptions during the thermal and structural modeling of the LPD process are as follows:

- The substrate is initially at room temperature (25°C). The boundary condition around the substrate is the convection heat transfer with a constant coefficient.
- The heat flux on the leading half of the molten pool (Fig. 3) has uniform distribution.
- The latent heat is considered in the temperature-dependent definition of specific heat.
- The activated elements of the molten pool are at the melting temperature. The convective redistribution of heat in the molten pool is ignored.
- The substrate is assumed to be stress free at the beginning of the process.
- The reference temperature for computing the thermal strain for the substrate and deposited material is the room temperature and melting temperature, respectively.
- The Z direction at the bottom of the substrate is subjected to zero constrained movement.

3 Results and discussion

It is predictable that changing the deposition pattern results in changing the temperature history of the process. The temperature contours of the part right after the last step of the deposition for different deposition patterns are shown in Fig. 7. As can be seen, the maximum temperature, just after turning off the laser, significantly drops below the melting temperature. This reduction is less in the short-bead pattern than in the other patterns.

Different temperature histories have a direct effect on the residual stress of the part. Figure 8 indicates the distribution of Von Misses stress after the part cools to room temperature. Except for the spiral-in pattern where the maximum residual stress is at the surface of the cladding layer, for the other patterns, it is at the interface of the cladding layer and the substrate. The short-bead pattern shows the lowest maximum residual stress among the patterns. In order to compare the stress at the top surface of the cladding layer, Table 3 summarizes the minimum and maximum stresses along x and y and the Von Misses stress. As indicated, the short-bead pattern has the minimum while the spiral-in pattern has the maximum equivalent stress.

To better understand the reason for the mentioned differences in the residual stress, a statistical study on the temperature distribution from the beginning (t=0 s) to the last step of the deposition process (t=15 s) for the four different deposition patterns is shown in Fig. 9. For every

Table 2 Structural properties of AISI 4140

Temperature (°C)	25	225	425	725	1,150	1,500
E (GPa)	200	180	160	140	40	1
σ_y (MPa)	875	785	700	610	175	4.5
α	1.04E-05	1.15E-05	1.18E-05	1.25E-05	1.40E-05	1.50E-05
ν	0.3	0.32	0.33	0.35	0.45	0.5

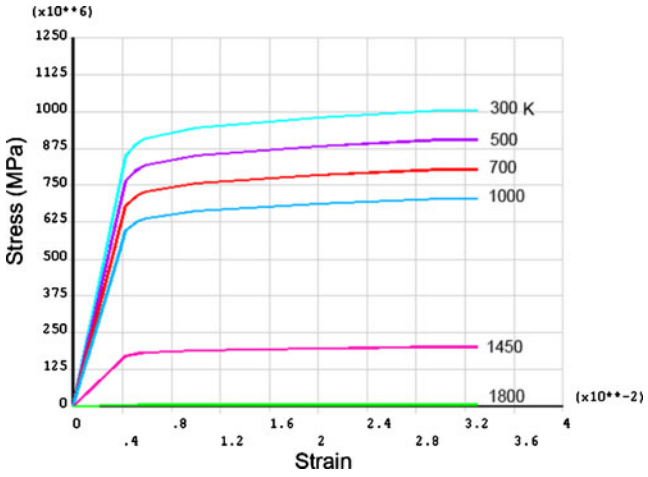

Fig. 6 Temperature-dependent stress-strain relation for AISI 4140

node on the surface of the deposited material in the finite element (FE) model, there is a temperature history that shows the temperature of the node during the processing time. Collecting the whole data of the nodes on the surface during the time interval of t=0-15 s and sorting them based on temperature ranges make the distributions shown in Fig. 9. Therefore, the vertical axis is the number of data that are collected in the corresponding temperature range shown in the horizontal axis. A noticeable difference is observed in Fig. 9 by comparing the different deposition patterns. As can be seen, the short-bead pattern has the narrowest and the spiral-in pattern has the widest band among the patterns. A narrow band histogram means less temperature variation and a wideband histogram means more temperature variation during the studying period. The non-uniformity of the temperature field is one of the main reasons for stress rising [32]. The long-bead and spiral-out patterns show a

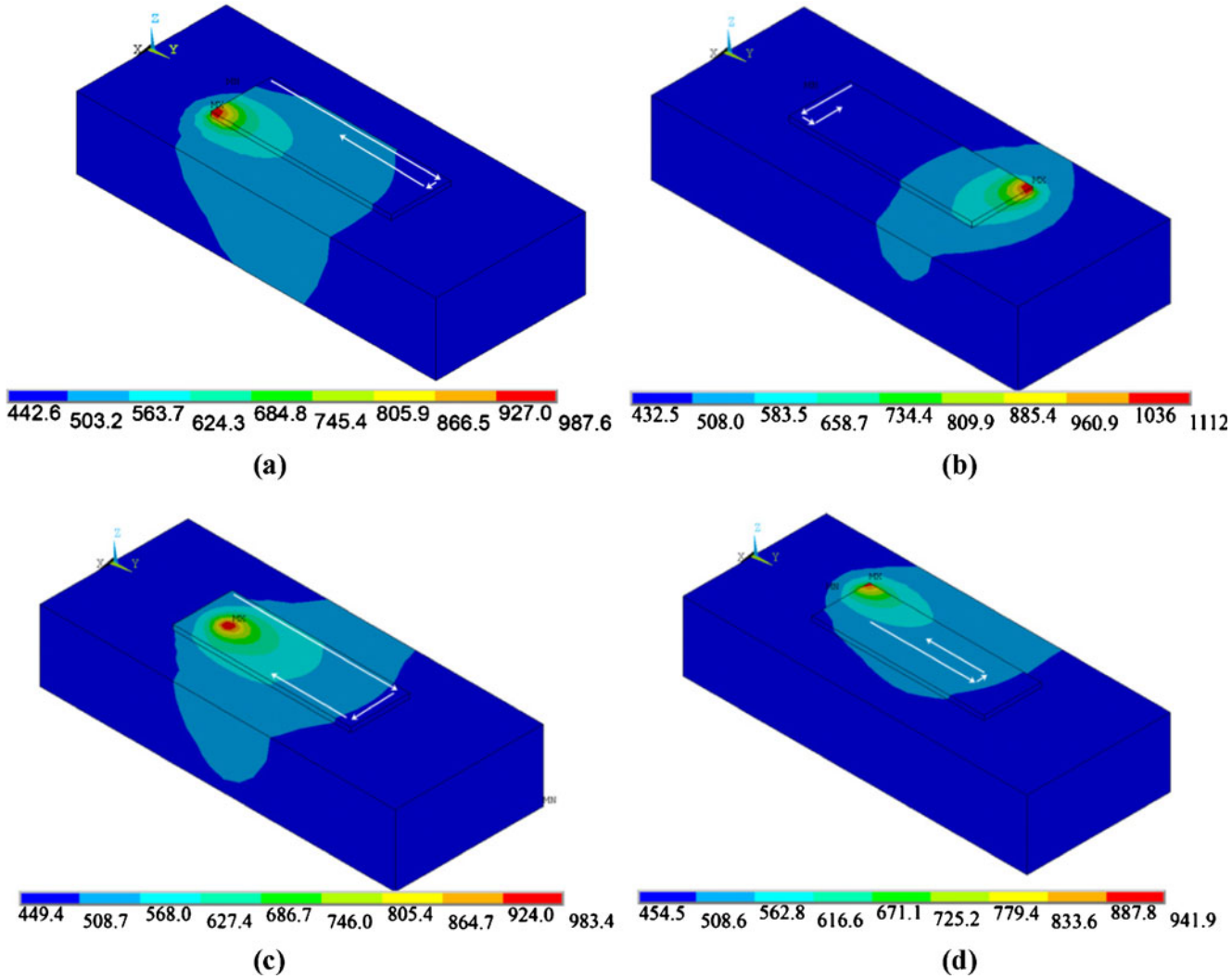

Fig. 7 Temperature distribution of the cladding layer in Kelvin right after the last deposition step; **a** long bead, **b** short bead, **c** spiral in, **d** spiral out

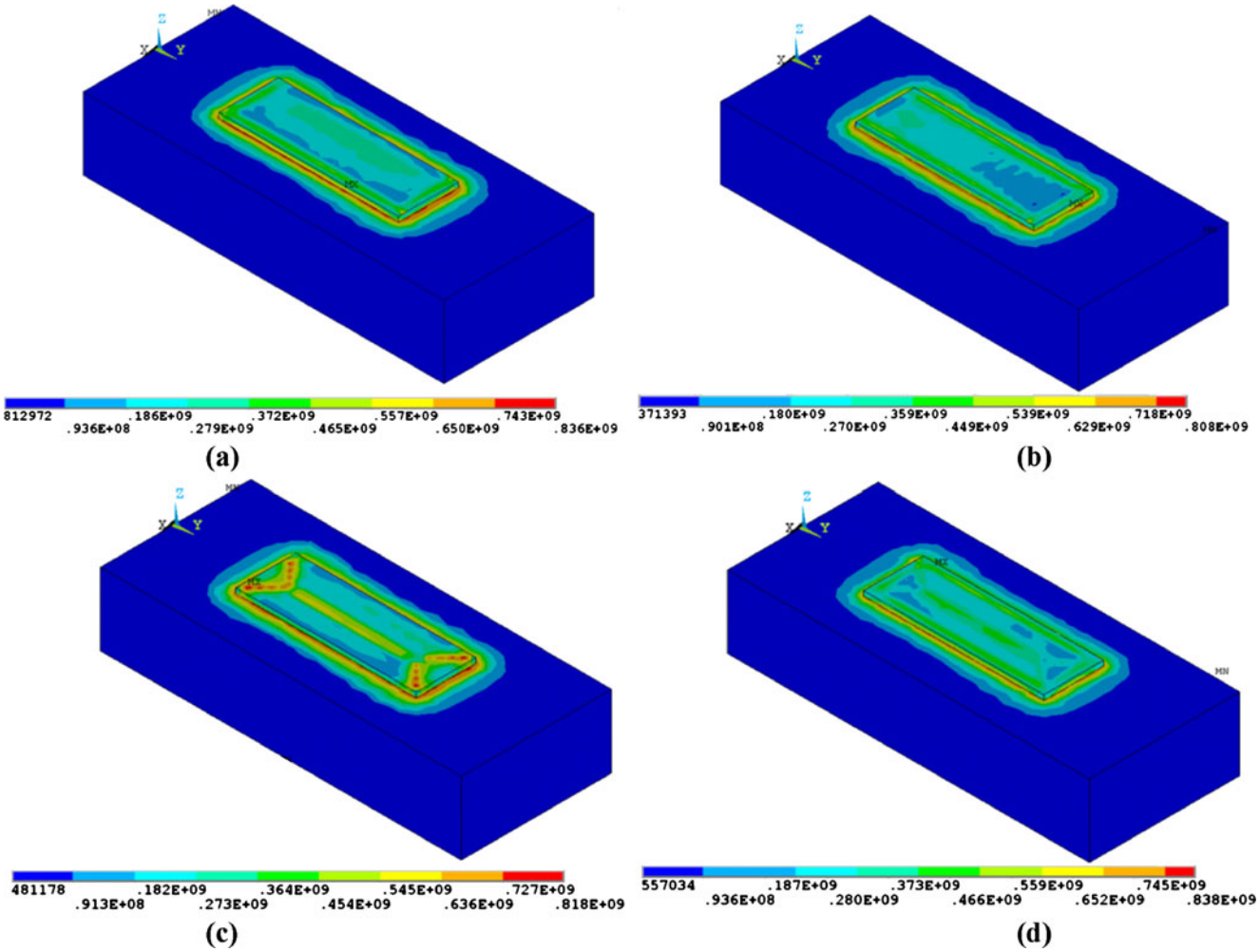

Fig. 8 Von Misses residual stress; **a** long bead, **b** short bead, **c** spiral in, **d** spiral-out pattern

similar shape of the histogram. The average temperature of the surface from the beginning of the process (t=0) to the last step of deposition (t=15) is shown in Table 4 for each deposition pattern. As can be seen, the spiral-in pattern has the minimum average temperature as opposed to the short-bead pattern that has the maximum average temperature. It can be concluded from Fig. 9 and Table 4 that more non-uniformity in the temperature field and a lower average temperature during the LPD process result in a higher residual stress in the deposited material. This result is similar to what was mentioned in the other sources about the effect of preheating the substrate to minimize the temperature variation and residual stress [11, 15].

Previous study by the authors [26] about the effect of path planning on the microstructural transformations and hardness distribution during the LPD process shows that the short-bead pattern has a relatively uniform hardness distribution with a higher average hardness than the other patterns. The long-bead and spiral-out patterns also show a relatively uniform hardness distribution, but with a less average hardness than the short-bead pattern. The spiral-in pattern, however, shows the most non-uniform hardness distribution. Comparing what mentioned with the results of the current study, it can be concluded that short-bead pattern has less residual stress and higher surface hardness than the other patterns.

Table 3 Min and max stresses of the surface of the deposited material

		S_x (MPa)	S_y (MPa)	S_{VM} (MPa)
Long bead	Min	−625	−487	30.7
	Max	240	358	593
Short bead	Min	−376	−447	69
	Max	184	394	531
Spiral in	Min	−445	−185	107
	Max	355	463	817
Spiral out	Min	−449	−373	92
	Max	521	368	547

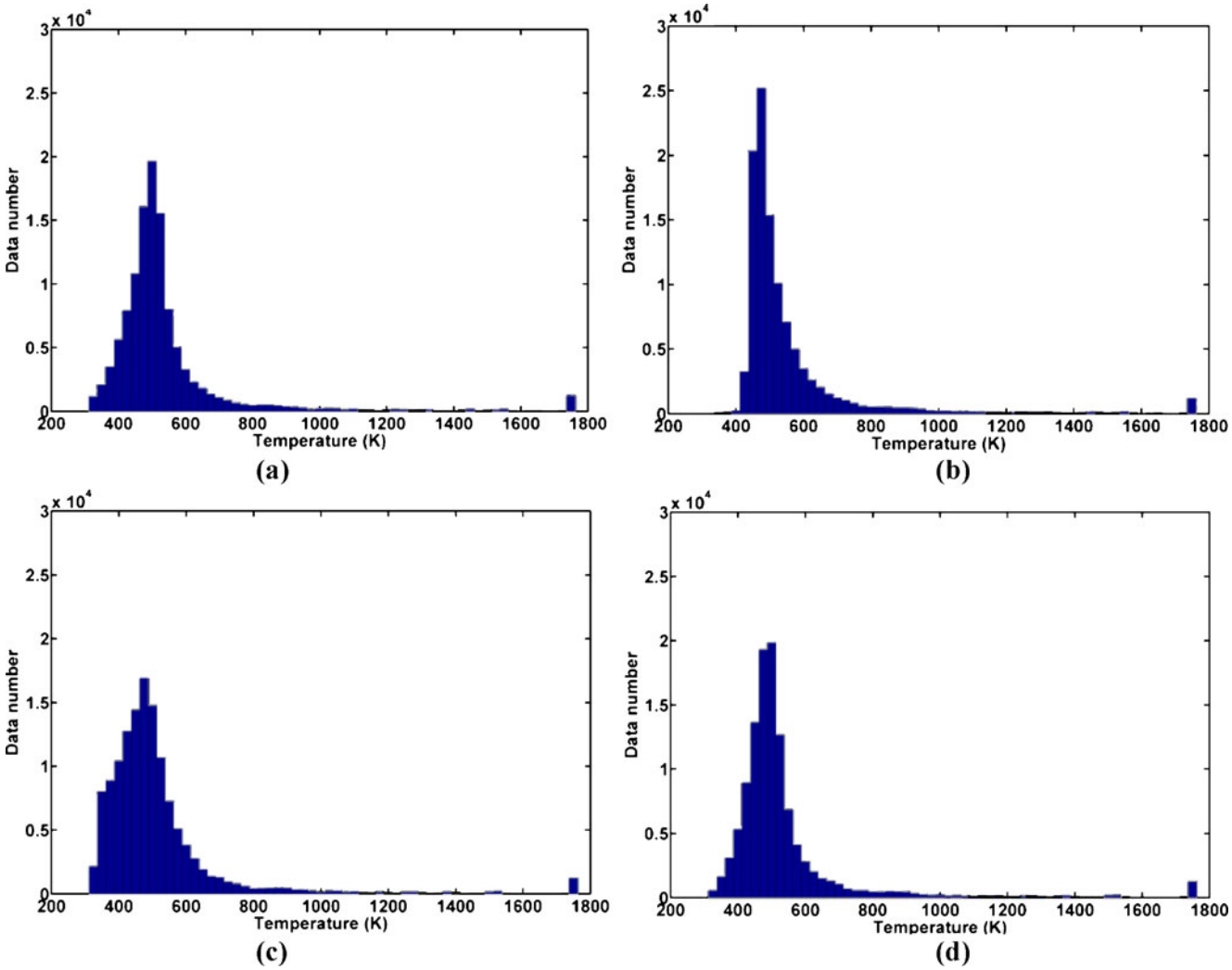

Fig. 9 Histogram of temperature vs. data number for different deposition patterns; **a** long bead, **b** short bead, **c** spiral in, **d** spiral out

It should be noted that in order to investigate the effect of mesh size on the final results, the FE model is analyzed with different mesh concentrations. It is revealed that increasing the number of elements by 2.7 and 7.9 times more than the presented model will yield a minor change of 1.3% and 1.7%, respectively, in the thermal results. This effect on the computation time, however, is 3.5 and 7.5 times more than the presented model, respectively. Therefore, the presented results are considered to be mesh-size independent and reliable.

4 Experimental verification

In order to verify the thermal-structural model and evaluate the predicted values of the stresses, a series of experiments are performed. The experimental setup consists of a 1-kW continuous wave Nd:YAG laser system assisted with a deposition head, a five-axis CNC vertical machining center, and a powder feeding system with argon carrying gas. Each coupon is placed on the workstation so that its expansion is unconstrained. The deposition patterns are defined in the CNC machine, and the process parameters (laser power, laser scanning speed, powder feeding rate, and spacing between tracks) are the same as the ones assumed in the model. Figure 10 shows the coupons for different deposition patterns. To evaluate the thermal model, a thermocouple is used to measure the surface temperature of the substrate. Figure 11 shows the attached thermocouple to the long-bead pattern sample. The measured and predicted data are compared in Fig. 12. As can be seen, the modeled temperature coincides very well with the measured one.

Table 4 Average temperature of the surface from t=0-15 s

	Long bead	Short bead	Spiral in	Spiral out
Temperature (K)	537.9	553.3	511.0	532.4

In order to evaluate the structural model, an X-ray residual stress measurement technique is adopted. The LXRD© stress measurement system from PROTO Manufacturing [33] is used with a Cr radiation source to measure the residual stress of the top surface of the deposited material. The detectors are set for the brag angle of 156° and from −30° to 30°, 11 tilt (ψ) angles evenly spaced are used to finally determine the d-spacing versus $\sin^2(\psi)$ curve. The data are analyzed using XRDWin 2.0 software to calculate the stress values. An aperture of 0.5 mm in diameter is used to confine the X-ray radiation area on the coupon. The preliminarily results show that the roughness of the surface due to unmelted particles would scatter the data. Therefore, the coupons are slightly electro-polished in order to make the surface of the deposited material smoother without inducing any stress or significantly removing the material. Five regions are assigned for the stress measurement along the dashed line shown in Fig. 10 for each sample. Three sets of measurement along each direction (SX and SY) are obtained to measure the average stress at each region. The results are shown in Figs. 13, 14, 15, and 16.

As can be seen in the above figures, the measured and modeled data have a close agreement for both the *X* and *Y* directions. As shown in Fig. 13a, a high compressive stress region presents about the last beads of the deposition pattern. A similar result can be seen by comparing Figs. 15a and 16a for the spiral-in and spiral-out patterns, respectively. It is worth noting that the deposition direction for the long-bead, spiral-in, and spiral-out patterns is along the *Y* axis. This direction for the short-bead pattern, however, is along the *X* direction. Therefore, the dashed lines shown in Fig. 10 along which the measurements are performed cross the last bead of the long-bead, spiral-in, and spiral-out, but not the short-bead pattern. Therefore, the short-bead pattern does not show the high compressive stress region along the measurement line. Nonetheless, the compressive stress is expected for the short-bead pattern in the last beads of the deposition process.

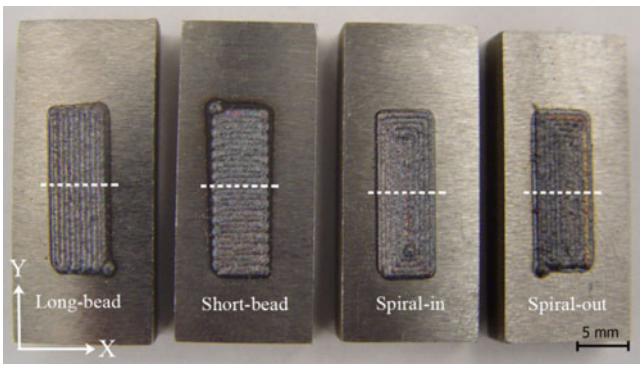

Fig. 10 Coupons made with different deposition patterns

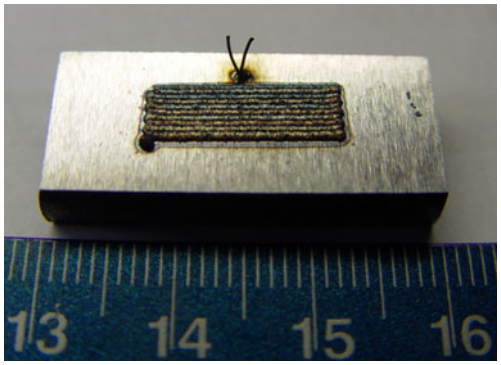

Fig. 11 Thermocouple attachment on long bead pattern sample

A more careful comparison between the measured and modeled data reveals some slight deviations at the regions with higher stresses. These deviations can be explained by considering the uncertainties present in the material model. In addition, although electro-polishing the surface of the coupons can remove the unmelted particles on the surface and make the surface smoother, the uneven surface of the deposited material because of the deposition beads can cause some missing data to occur during the measurements. Nonetheless, the agreement between the predicted residual stress values and the measured ones is close enough to prove the mentioned conclusions about the effect of the deposition pattern on the final stress distribution.

5 Conclusions

One of the process parameters of the LPD process in surface modification is the deposition pattern. The deposition pattern can change the temperature history of the process, and consequently, change the final properties of the deposited material. In this study, the effect of four deposition patterns on the residual stress distribution of the deposited material is investigated. The results show that

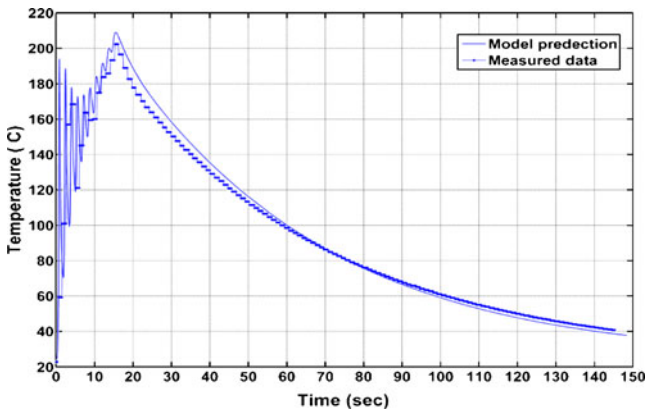

Fig. 12 Comparison of the predicted and measured data of the model

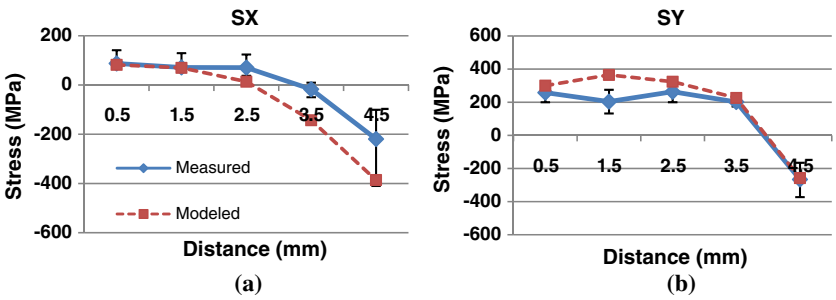

Fig. 13 Comparing the measured and modeled data for long-bead pattern; **a** SX, **b** SY

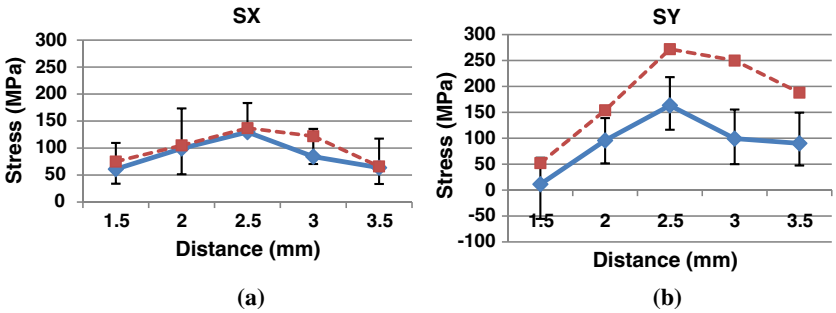

Fig. 14 Comparing the measured and modeled data for short-bead pattern; **a** SX, **b** SY

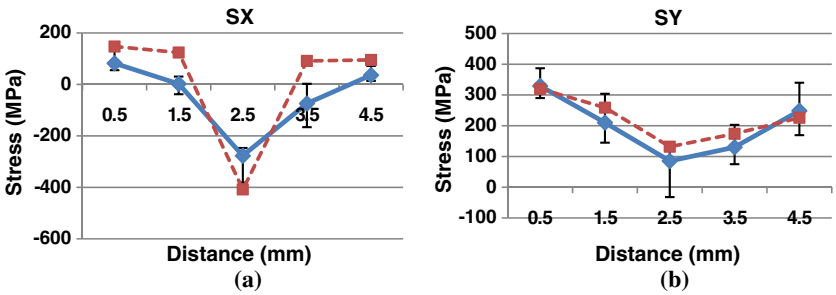

Fig. 15 Comparing the measured and modeled data for spiral-in pattern; **a** SX, **b** SY

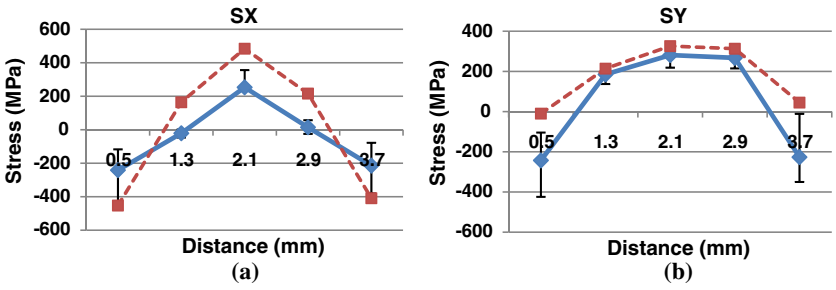

Fig. 16 Comparing the measured and modeled data for spiral-out pattern; **a** SX, **b** SY

among the four deposition patterns, the short-bead pattern has less temperature variation and a higher average temperature during the deposition process. The spiral-in pattern, however, shows a larger temperature variation and lower average temperature during the deposition process. The stress analysis shows that the short-bead pattern has the minimum and the spiral-in pattern has the maximum residual stress in the deposited material. The modeled residual stresses are compared with the experimental ones and a close agreement is obtained.

Acknowledgment This work was financially supported by NSF Grant No. EEC-0541952.

References

1. Kovacevic R (2006) System and method for fabrication or repairing part. US Patent #7,020,539
2. Kovacevic R, Hu D, Valant M, (2007) System and method for controlling the size of the molten pool in laser-based additive manufacturing. US patent #6,995,334 B1
3. Toyserkani E, Khajepour A, Corbin SF (2006) System and method for intelligent closed-loop control of laser cladding by powder injection. Granted US patent #7043330
4. Choi J, Chang Y (2005) Characteristics of laser aided direct metal/material deposition process for tool steel. Int J Mach Tools Manuf 45:597–607
5. Choi J, Hua Y (2004) Dimensional and material characteristics of direct deposited H13 tool steel by CO_2 laser. J Laser Appl 16–4:245–251
6. Ghosh S, Choi J (2007) Deposition pattern based thermal stresses in single-layer laser-aided direct material deposition process. J Manuf Sci Eng Trans ASME 129:319–332
7. Kahlen FJ, Kar A (2001) Residual stress in laser-deposited metal parts. J Laser Appl 13–2:60–69
8. Deus AM, Mazumder J (1996) Two-dimensional thermo-mechanical finite element model for laser cladding. Proc ICALEO96, Orlando, FL B/174-B/183
9. Vasinonta A, Beuth JL, Griffith ML (1999) Process maps for laser deposition of thin-walled structures. Proc 1999 Solid Freeform Fabrication Symp, Austin, TX, ed. Bourel et al, 383–391
10. Vasinonta A, Beuth JL, Griffith ML (2000) Process maps for controlling residual stress and melt pool size in laser-based SFF processes. Proc 2000 Solid Freeform Fabrication Symp, Austin, TX ed. Bourel et al 383–391
11. Labudovic M, Hu D, Kovacevic R (2003) A three-dimensional model for direct laser metal powder deposition and rapid prototyping. J Mater Sci 38-1:35–49
12. Dai K, Shaw L (2001) Thermal and stress modeling of multi-material laser processing. Acta Mater 49:4171–4181
13. Costa L, Reti T, Deus AM, Vilar R (2002) Simulation of layer overlap tempering kinetics in steel parts deposited by laser cladding. Proc 2002 Intrl Conf. Metal Powder Deposition Rapid Manuf San Antonio, TX ed. D. Keicher et al. 172–179
14. Costa L, Deus A.M, Reti T, Vilar R (2002) Simulation of layer overlap tempering in steel parts produced by laser cladding. Jorge J et al (ed) Proc RPD 2002 Advanc Solu Devel Marinha Grande, Portugal
15. Jendrzejewski R, Sliwinski G, Krawczuk M, Ostachowicz W (2004) Temperature and stress fields induced during laser cladding. J Comput Struct 82:653–658
16. Bendeich P, Alam N, Brandt M, Carr D, Short K, Blevins R, Curfs C, Kirstein O, Atkinson G, Holden T, Rogge R (2006) Residual stress measurements in laser clad repaired low pressure turbine blades for the power industry. J Mater Sci Eng A 437:70–74
17. Richter KH, Orban S, Nowotny S (2004) Laser cladding of the titanium alloy Ti6242 to restore damaged blades. Proc 23rd Interl Congress Appl Lasers Electro-Optics
18. Nickel AH, Barnett DM, Prinz FB (2001) Thermal stresses and deposition patterns in layered manufacturing. J Mater Sci Eng A 317:59–64
19. Plati A, Tan JC, Golosnoy IO, Persoons R, Acker K, Clyne TW (2006) Residual stress generation during laser cladding of steel with a particulate metal matrix composite. J Adv Eng Mater 8–7:619–624
20. Neela V, De A (2007) Numerical modeling of LENS process using special element features. Proc 2007 Abaqus India Regional Users' Meet
21. Gosh S, Choi J (2006) Modeling and experimental verification of transient/residual stresses and microstructure formation in multi-layer laser-aided DMD process. J Heat Trans 128–7:662–679
22. Ghosh S, Choi J (2007) Deposition pattern based thermal stresses in single-layer laser-aided direct material deposition process. J Manuf Sci Eng 129:319–332
23. Ghosh S, Choi J (2004) Three-dimensional transient finite element analysis for microstrucutre formation and residual stress in laser-aided DMD process. Proc 2004 ASME Heat Transfer/Fluids Eng Summer Conf, Charlotte, NC: 969–978
24. Mochizuki M, Toyoda M (2007) Strategy of considering micro-structure effect on welding residual stress analysis. J Pressure Vessel Technol Trans ASME 129:619–629
25. Borjesson L, Lindgren LE (2001) Simulation of multipass welding with simultaneous computation of material properties. J Eng Mater Technol 123:106–111
26. Foroozmehr E, Kovacevic R (2009) Thermo-kinetic modeling of phase transformation in laser powder deposition. Metall Mat Trans A Phys Metall Mat Sci 40–8:1935–1943
27. Documentation for ANSYS, Release 11.0, Ch. 13, Element birth and death
28. Sarrafi R, Lin D, Kovacevic R (2009) Surface treatment by variable-polarity arc to promote the energy absorption in laser welding of aluminum alloy Proc TMS 2009, San Francisco, CA
29. Neto O, Vilar R (2002) Physical computational model to describe the interaction between a laser beam and a powder jet in laser surface processing. J Laser Appl 14–1:46–51
30. Totten G, Howes M, Inoue T, Handbook or residual stress and deformation of steel, ASM International
31. Documentation for ANSYS, Release 11.0, Ch. 4, Structures with material nonlinearities
32. Wang G, Chen Y, Zhang H (2003) Effect of scanning path on the deposition process in rapid plasma spray tooling: modeling by homogenization theory. J Thin Solid Films 435:124–130
33. PROTP Manufacturing. http://www.protoxrd.com/lxrd.htm. Accessed June 2009